

# Near-Infrared Light-Activated Oxygen Generator a Multidynamic Photo-Nanoplatfor m for Effective Anti-Cutaneous Squamous Cell Carcinoma Treatment

Xin Zhang<sup>1,3</sup>, Xiangbo Bu<sup>4</sup>, Wenyu Jia<sup>1,2</sup>, Yu Ying<sup>1,2</sup>, Shanrong Lv<sup>1,2</sup>, Guan Jiang<sup>1,2</sup> 

<sup>1</sup>Department of Dermatology, the Affiliated Hospital of Xuzhou Medical University, Xuzhou, Jiangsu, 221002, People's Republic of China;

<sup>2</sup>Department of Clinical Medicine, Xuzhou Medical University, Xuzhou, Jiangsu, 221004, People's Republic of China; <sup>3</sup>Department of Dermatology, Xuzhou Children's Hospital, Xuzhou Medical University, Xuzhou, Jiangsu, 221000, People's Republic of China; <sup>4</sup>Department of Orthopaedics, Xuzhou Central Hospital, Xuzhou Clinical School of Xuzhou Medical University, Xuzhou, Jiangsu, 221009, People's Republic of China

Correspondence: Guan Jiang, Email dr.guanjiang@xzhmu.edu.cn

**Introduction:** Nanophototherapy has emerged as a novel and promising therapeutic strategy for cancer treatment; however, its efficacy in dermatological tumors and precancerous lesions remains severely limited. This study aimed to use the gas-liquid injection technique to fully utilize the synergistic photodynamic therapy (PDT)/photothermal therapy (PTT) of nanomaterials to enhance the antitumor effect.

**Methods:** A novel oxygen-generating nanocomposite (TSL-IR820-CAT) was synthesized by encapsulating the photosensitizer IR820 and catalase (CAT) using a matrix encapsulation method based on thermosensitive liposomes (TSL).—The liquid injection technology enhances the treatment of cutaneous squamous cell carcinoma (cSCC). The combined PDT/PTT therapeutic effect of TSL-IR820-CAT on cSCC was investigated using in vivo and in vitro experiments.

**Results:** TSL-IR820-CAT, with good stability, efficient drug release, and photothermal conversion ability, was successfully developed. Nanoparticles injected through a needle-free syringe efficiently accumulate in the tumor tissue. As TSL-IR820-CAT was consumed by A431 cells, some of it localized to the mitochondria and produced oxygen to relieve hypoxia, thereby enhancing the efficacy of PDT. PDT/PTT combination therapy resulted in irreversible apoptosis and inhibited cSCC growth. TSL-IR820-CAT coupled with gas-liquid injection was free from apparent systemic side effects.

**Conclusion:** This article discusses new strategies and ideas for treating skin tumors and has significant application value.

**Keywords:** skin squamous cell carcinoma, nanoparticles, gas-liquid injection technology, photodynamic therapy, photothermal therapy

## Introduction

Nanophototherapeutic systems have attracted growing interest as an effective cancer treatment strategy and have made considerable progress in recent years, offering a unique combination of non-invasiveness, precision, and low systemic toxicity as an opportunity to eliminate cancer.<sup>1-4</sup> The delivery of drugs and illumination are critical components of a tumor therapy platform. Nanomaterials are often injected into the tail vein, and passive targeted delivery results from the high permeability retention effect (EPR) after blood circulation reaches the site of the solid tumor.<sup>5</sup> Although EPR is effective for accumulating drugs at the tumor site, it has the potential to deliver only a limited number of anticancer agents to tumor tissues, thereby impairing the therapeutic effect of current nanophototherapy systems.<sup>6,7</sup> Most in vivo experiments are conducted using a mouse subcutaneous tumor model, which produces tumors visible to the naked eye.<sup>8,9</sup> Choosing a light source with a specific tissue penetration depth is important.

Gas-liquid injection technology uses a needle-free syringe close to the injection site and creates a high-speed jet (often exceeding 100 m/s) with the aid of instantaneous high pressure. This ensures that the drug penetrates directly the skin and diffuses into the subcutaneous, intradermal, and mucosal tissues.<sup>10</sup> By pressing the trigger of a German INJEX needleless syringe, the drug diffuses into the subcutaneous layer in less than 2 s under 3000 psi, with a penetration depth of approximately 5–8 mm.<sup>11</sup> Needle-free injections can reduce the loss and aid in pushing them through the skin barrier, allowing them to diffuse more quickly into the target tissue.

Additionally, the stratum corneum forms a major component of the skin barrier, and hyperkeratosis is often seen in cutaneous squamous cell carcinoma (cSCC) and its precancerous lesions,<sup>12</sup> making it difficult for light sources to penetrate the skin barrier effectively to reach tumor cells. Near-infrared (NIR) light offers certain advantages, such as guaranteeing a specific penetration depth and minimizing tissue damage.<sup>13,14</sup> Thus, the cherry on top integrates gas-liquid injection technology into a nanophototherapy platform and treating patients with NIR laser radiation.

In addition to photodynamic therapy (PDT), photothermal therapy (PTT) is a known phototherapy method.<sup>15,16</sup> PDT relies on a specific wavelength of excitation light to irradiate a photosensitizer (PS) in the presence of molecular oxygen to generate singlet oxygen (ROS) and other reactive oxygen species, causing tumor cell necrosis and apoptosis.<sup>17,18</sup> However, insufficient penetrating photosensitizers and low oxygen levels prevent photodynamic reactions from working efficiently.<sup>19–21</sup> Photothermal therapy (PTT) converts light energy into heat using photothermal conversion agents (PTCAs), and the resulting heat energy destroys tumor tissue.<sup>22,23</sup> Although PTT appears to be a promising and highly effective tumor therapy, it suffers from heat inhomogeneity in the tumor, which can lead to tumor recurrence.<sup>24</sup> Therefore, PDT or PTT cannot treat skin cancer effectively as a single therapy.<sup>25,26</sup> Together, PDT and PTT can offer synergistic treatment effects.

This study used gas-liquid injection technology to develop a synergistic antitumor nanotherapeutic system (TSL-IR820-CAT). The nanoparticles take thermosensitive liposomes (TSL) as carriers, and catalase (CAT) and IR820 are added, thereby exerting a synergistic antitumor effect through oxygen generation combined with photosensitivity and photothermal effects. This system uses needle-free injection technology to facilitate the penetration of TSL-IR820-CAT through the skin barrier, where it can rapidly diffuse and accumulate in the tissue of interest. Rapid diffusion, followed by rapid penetration, has become a key point in the actual transformation at this stage. TSL is a novel tumor-targeted drug carrier whose EPR in tumor vessels can be enhanced by local heating.<sup>27,28</sup> The phospholipids that make up the TSL membrane are sensitive to temperature, and when the temperature exceeds the phase transition temperature ( $T_m$ ), the liposome membrane transitions from the “colloidal crystal state” to the “liquid crystal state.” TSL effectively utilizes the dual advantages of liposomes and hyperthermia to improve the efficacy of cSCC treatment and reduce toxic side effects.<sup>29,30</sup> CAT boosts the effectiveness of PDT by producing oxygen in tumor tissue. IR820 has a dual identity. As PTCA, it has strong NIR absorption and photothermal conversion ability, and as PS, it can generate more ROS under NIR excitation to enhance the effect of PDT.<sup>31</sup> Using a single 808 nm near-infrared light source can also penetrate deeper tissue layers (the penetration depth is approximately 5–10 mm), thoroughly ensuring the excitation of nanomaterials embedded within tumors.<sup>32</sup> In this study, we conducted *in vitro* and *in vivo* studies to validate the high performance of our intelligent and straightforward tumor therapy platform.

## Materials and Methods

### Synthesis of TSL-IR820-CAT

A matrix packaging strategy was used to prepare IR820-TSL-CAT.<sup>33</sup> First, 3 mg of IR820 was accurately weighed, added to 11 mL of pure water, and sonicated for 3 min until the substance was thoroughly mixed. A mixture containing 30 mg of DPPC, 3 mg DSPE, 1 mg DSPE-mPEG2000, and 3.2 mg MSPC was weighed and dissolved in 8 mL of methanol and sonicated for 3 min to dissolve fully. Then, the IR820-H<sub>2</sub>O mixture was transferred into a 50 mL eggplant-shaped bottle and placed on a magnetic stirrer for stirring at 230 rpm at a temperature of 30 °C. The 8 mL methanol solution containing DPPC, DSPE, DSPE-mPEG2000, and MSPC was slowly added dropwise to the eggplant flask. The mixture was stirred overnight at 30 °C in the dark to remove methanol components. The next day, 1.2 mg of CAT was dissolved in 1 mL of pure water, added to the eggplant-shaped bottle mentioned

previously, and hydrated for 1 h. Phacoemulsification (30%, 2 min) was performed using a sonicator (900 W) and repeated six times. The mixture was then passed through 0.45-, 0.22, and 0.10  $\mu\text{m}$  filter membranes in sequence and repeated six times. A refrigerated centrifuge (4 °C, 4600 rpm, and 30 min) was used to separate the pellet from the solution. PBS (4 mL) was added to resuspend the pellet to obtain IR820-TSL-CAT, stored in a refrigerator at 4 °C.

TSL-IR820, calcein-TSL-IR820 (c-TINP), and coumarin 6-TSL-IR820-CAT (f-TICNP) were prepared according to the above synthetic method, except that CAT was not added to the processor in step 1 except by adding 2 mg of calcein in pure water, or by adding 3 mg of coumarin 6 to methanol in step 2, the rest steps were not changed. c-TINP was used for drug release experiments, while f-TICNP was used for cell uptake, intracellular colocalization, and animal in vivo imaging experiments.

## Characterization of TSL-IR820-CAT

The particle size, morphology, and stability of TSL-IR820-CAT were observed using transmission electron microscopy (Tecnai G2 T12, FEI, USA). The particle size distribution was characterized using a laser particle size analyzer (Zetasizer Nano ZS90, Malvern, UK). A multifunctional microplate reader (NanoDrop One, Thermo, USA) was used to measure the amount of CAT encapsulated in liposomes at 562 nm. The ultraviolet absorption curves of CAT, IR820, and TSL-IR820-CAT were recorded using an ultra-micro spectrophotometer (Multiskan GO, Thermo, USA). Standard concentration curves of free IR820 and calcein were plotted by recording different concentrations of IR820 or calcein to determine the amount encapsulated in liposomes at 780 and 497 nm, respectively. The encapsulation rate was calculated as follows: encapsulation rate (%) = actual drug content/initial addition amount  $\times$  100%.

## Drug Release of Calcein-TSL-IR820

The release rate of TSL-IR820-CAT triggered by a near-infrared laser was investigated using calcein release experiments.<sup>34</sup> According to the step mentioned above, 2.3, the concentration of the drug was calculated to obtain the standard curve of calcein. Calcein-coated c-TINP and c-TNP in PBS were incubated in a 96-well plate, treated with 4% Triton X-100, or irradiated with an 808 nm laser (1.5 W/cm<sup>2</sup>) for different periods (0–10 min). The time-dependent release rate calculation formula for c-TINP and c-TNP was triggered by an 808 nm laser:  $E_R = [(C_R - C_b)/(C_t - C_{bt})] \times 100\%$ .  $C_R$  is the concentration of calcein released from c-TINP or c-TNP triggered by a near-infrared laser,  $C_b$  is the background concentration,  $C_t$  is the concentration of calcein released from c-TINP or c-TNP treated with Triton X-100, and  $C_{bt}$  is the background concentration after adding Triton X-100.

## In vitro Photothermal Properties of TSL-IR820-CAT

TSL-IR820-CAT solutions containing IR820 at concentrations of 50, 75, 100, and 125  $\mu\text{g/mL}$  were added to a quartz cuvette. TSL-IR820-CAT solutions of different concentrations were irradiated with near-infrared light (1.5 W/cm<sup>2</sup>) at a wavelength of 808 nm for 6 min. A TSL-IR820-CAT solution with the same concentration as IR820 (125  $\mu\text{g/mL}$ ) was prepared. One mL of each was added to a small quartz cell, and 808 nm near-infrared light with energy intensities of 0.75, 1, 1.25, 1.5, and 1.75 W/cm<sup>2</sup> was used for irradiation for 6 min. The temperature changes at different irradiation times were tracked using a non-contact infrared thermal imager (Fotric 220s, USA).

## A431 Cell Culture and Tumor-Bearing Nude Mouse Model

The human skin squamous cell carcinoma cell A431 was obtained from Procell Life Science & Technology Co., Ltd. and cultured in a high-glucose DMEM medium (10% FBS and 1% penicillin-streptomycin solution). When the cells were 90% confluent, they were subcultured at a 1:2 ratio for use in cell experiments and the establishment of tumor models. All animals were purchased from the Charles River Laboratory Animal Technology Co., Ltd. Animal experiments were examined and verified by the Laboratory Animal Ethics Committee of Xuzhou Medical University and conducted following the Experimental Animal Center of Xuzhou Medical University on animal welfare guidelines (approval number L20210226072). 4–6-week-old female BALB/c-nu nude mice were housed in an SPF-level barrier system. To construct the tumor-bearing nude mouse model, the A431 cell suspension ( $5 \times 10^7$  cells/mL, 100  $\mu\text{L}$ ) was subcutaneously

injected into the right armpit of BALB/c nude mice. Tumor volume calculation method:  $V \text{ (mm}^3\text{)} = (d^2 \times D)/2$ , where  $d$  represents the short diameter of the tumor and  $D$  represents the long diameter of the tumor (mm).

## Cytotoxicity Assay

A431 cell suspension ( $2 \times 10^4$  cells/well) was seeded in a 96-well plate. After overnight culture, each well was added to a mixed medium containing different concentrations of TSL-IR820-CAT (0, 25, 50, 75, 100, 125, and 150  $\mu\text{g/mL}$ ) according to the groups. Each group was provided six parallel holes. After 24 h of incubation, 10  $\mu\text{L}$  of CCK-8 solution was added to each well, and the cells were incubated in the dark for 30 min. The absorbance of the mixed solution in each well at a wavelength of 450 nm was measured using a microplate reader, and the experimental results were recorded simultaneously.

## Cellular Uptake and Localization of Coumarin 6-TSL-IR820-CAT

A431 cells were seeded in 6-well plates at  $1 \times 10^5$  cells/well density. After cell adhesion, they were incubated with a complete medium containing different concentrations of f-TICNP (0, 50, and 100  $\mu\text{g/mL}$ ) for 4 h. The cells were washed thrice with PBS, and 1 mL of 4% paraformaldehyde was added to each well for 15 min. Then, 500  $\mu\text{L}$  of DAPI solution was used for nuclear staining. The results were observed and directly recorded using an inverted fluorescence microscope. Alternatively, the collected cells were analyzed by flow cytometry to determine the uptake of different concentrations of f-TICNP).

Cells ( $1 \times 10^4$  cells/well) were seeded in culture plates, specifically used for confocal observation, for 24 h. Medium containing 125  $\mu\text{g/mL}$  f-TICNP was added to each plate and incubated for 4 h. In the dark, cells were incubated in an HBSS solution containing MitoTracker Red for 20 min to label mitochondria or in an HBSS solution containing Lyso-Tracker Red for 40 min to label lysosomes. The cells were fixed with 4% paraformaldehyde. In the dark, mitochondrial or lysosomal localization results were observed by laser scanning confocal microscopy (Leica STELLARIS 5, Germany). (coumarin 6: excitation wavelength:466 nm, emission wavelength:504 nm; MitoTracker Red/Lyso-Tracker Red: excitation wavelength:579 nm, emission wavelength:599 nm).

## Oxygen Production Characteristics of TSL-IR820-CAT in Cells

A431 cells, after routine digestion, were seeded in a 6-well plate at a density of  $2 \times 10^5$  cells/well and incubated for 24 h. A fresh medium containing 5  $\mu\text{M}$   $[\text{Ru}(\text{dpp})_3] \text{Cl}_2$  was added to each well and incubated for 4 h. After rinsing with PBS, a medium (125  $\mu\text{g/mL}$ ) containing PBS, TSL-IR820, and TSL-IR820-CAT was added, with three replicate wells in each group, and incubated in the dark for 12 h. After fixation of the cells with 4% paraformaldehyde, DAPI solution was added for nuclear staining. Fluorescence images were obtained using a confocal laser microscope.

## Production of Intracellular ROS

The configured cell suspension ( $2 \times 10^5$  cells/well) was seeded into a 6-well plate. After 24 h of incubation, a complete medium containing PBS or TSL-IR820-CAT (125  $\mu\text{g/mL}$ ) was added to the corresponding group for 4 h of incubation, including the Control, Laser Only, TSL-IR820-CAT Only, Laser+TSL-IR820-CAT as PDT group, and Laser+TSL-IR820-CAT+ $\text{H}_2\text{O}_2$  as the PDT- $\text{H}_2\text{O}_2$  group. The mixture was washed three times with PBS to remove free drugs and floating cells. Subsequently, 20  $\mu\text{M}$  DCFH-DA dye was added to each well, and 50  $\mu\text{M}$  reactive oxygen species donor ( $\text{H}_2\text{O}_2$ ) was added to the positive group simultaneously. The cells were gently mixed to disperse them and incubated in the dark for 30 min. After washing with PBS, 1 mL of phenol red-free medium was added to the wells for each group that required laser irradiation and then irradiated with an 808 nm laser at a power of  $1 \text{ W/cm}^2$  for 10 min. Corresponding images of ROS production were acquired immediately using an inverted fluorescence microscope. In addition, flow cytometry was used to analyze the ROS production in the different groups.

## In vitro Synergistic Tumor Cell Ablation

To evaluate the effectiveness of TSL-IR820-CAT, it was divided into five groups (Control, Laser Only, PDT, PTT, and PDT+PTT). In the PDT group, laser irradiation was performed under ice incubation. A431 cells were pretreated with

vitamin C in the PTT group to remove ROS.<sup>35,36</sup> A431 cells were seeded in 6-well plates at a density of  $2.5 \times 10^5$  cells per well for 24 h. PBS and TSL-IR820 were added to the wells of control and PTT groups and incubated for 4 h, while TSL-IR820-CAT was distributed to PDT and PDT+PTT groups and incubated with cells for 4 h. Cells were placed under laser for 808 nm laser ( $1.5 \text{ W/cm}^2$ ) irradiation for 10 min and stained with a working solution of  $2 \mu\text{M}$  calcein-AM (live cells) and  $8 \mu\text{M}$  PI (dead cells) for 30 min. Observations were conducted under an inverted fluorescence microscope to assess the treatment effects.

## In vivo FI Imaging of Coumarin 6-TSL-IR820-CAT

After the subcutaneous tumors in nude mice reached approximately  $300 \text{ mm}^3$ , an f-TICNP solution ( $50 \mu\text{L}$ ) was instilled in vitro through a needleless syringe into the tumor-bearing mice. FI images were captured at 0.5, 2, 4, and 6 h using a small animal under visible light in an in vivo imaging system (PerkinElmer, USA). FI images collected before f-TICNP injection in tumor-bearing nude mice served as controls.

## Measurement of $\text{O}_2$ Production in vivo

Mice were randomly assigned to three groups of three mice each: control (control), TSL-IR820, and TSL-IR820-CAT. After the subcutaneous tumor in each group grew to approximately  $200 \text{ cm}^3$ , the drug was injected vertically into the tumor using a needle-free syringe. The TSL-IR820 and TSL-IR820-CAT groups were injected with  $50 \mu\text{L}$  of the corresponding nano-solution, and the control group was injected with  $50 \mu\text{L}$  of normal saline. After 24 h of needle-free injection, each group was sacrificed by dislocation, and the complete tumor was dissected and placed in 10% formaldehyde solution for 48 h of fixation. Photographs were taken and recorded using an inverted fluorescence microscope after immunofluorescence staining.

## In vivo Photodynamic Therapy and Photothermal Ablation

TSL-IR820-CAT was tested in 25 tumor-bearing mice to determine its therapeutic effect. Nude mice were randomly divided into five groups of five mice each after the tumor reached a size of approximately  $100 \text{ mm}^3$ . The experimental groups included the control, laser-only, PDT, PTT, and PDT+PTT groups. The control group was injected with  $50 \mu\text{L}$  normal saline using a needleless syringe (1). In the laser-only group,  $50 \mu\text{L}$  normal saline was injected using a needleless syringe. The tumor area was irradiated with an 808-nm laser transmitter for 10 min (power density of  $1.5 \text{ W/cm}^2$ ) (2). In the PDT group,  $50 \mu\text{L}$  of TSL-IR820-CAT suspension with  $125 \mu\text{g/mL}$  concentration was injected through a needleless syringe. Then an 808-nm laser was irradiated at a power density of  $1.0 \text{ W/cm}^2$  for 10 min (3). The PTT group was injected with a TSL-IR820 suspension ( $50 \mu\text{L}$ ,  $125 \mu\text{g/mL}$ ) through a needleless syringe and then irradiated with an 808 nm laser ( $1.5 \text{ W/cm}^2$ ) for 10 min (4). In the PDT + PTT group, TSL-IR820-CAT suspension ( $50 \mu\text{L}$ ,  $125 \mu\text{g/mL}$ ) was injected with a needleless syringe, and then laser irradiation was performed at a power density of  $1.5 \text{ W/cm}^2$  for 10 min (5).

In mice, tumor growth was assessed by measuring the tumor diameter and length two days per week for 18 days after suspension and irradiation were administered. After 24 h of treatment in each group, the tumor site was dissected from each mouse, and histopathological analysis was performed using H&E and TUNEL staining.

The control, PDT, and PDT + PTT groups received another mouse, and when the subcutaneous tumor grew to approximately  $300 \text{ mm}^3$ , each group received the corresponding treatment plan. The control group obtained near-infrared thermal images and temperature information of the tumor area at each time point (0–7, and 10 min); a thermal imager recorded PDT and PDT + PTT groups.

## In vivo Toxicity Assessment

The growth of mice was reflected in their weights at two days per week. After the 18-day treatment cycle of 25 mice, the mice were sacrificed, and major organs (heart, liver, spleen, lung, and kidney) were removed for H&E staining.

## Statistics

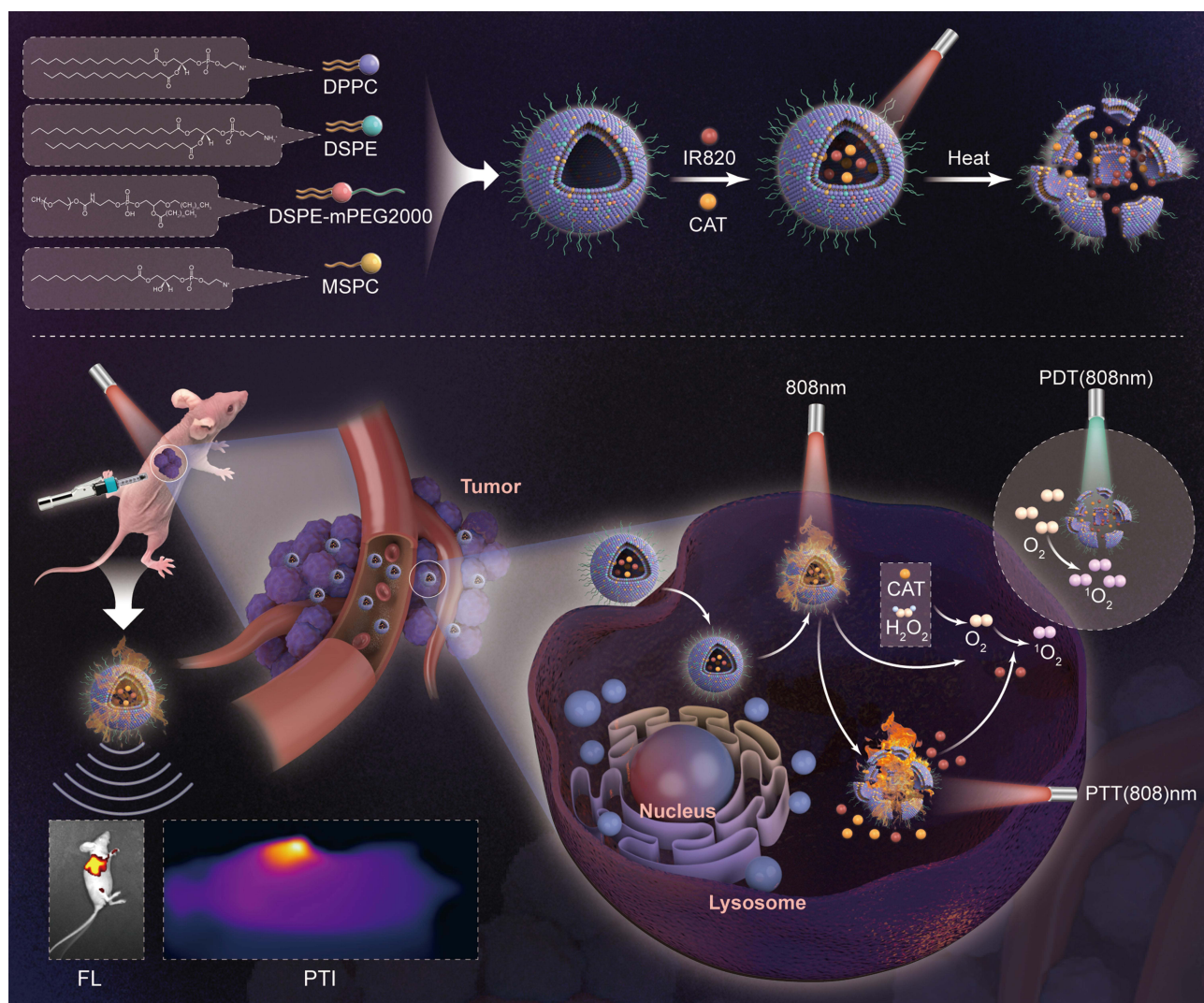
All statistical analyses were performed using SPSS 22.0. Measurement data are presented as mean  $\pm$  standard deviation. \* $P < 0.05$ , minimum level of significance of the data.

## Results and Discussion

### Synthesis and Characterization of TSL-IR820-CAT

There has been a growing interest in nanomedicine owing to its unique functionality and controllability, and it has become a hot research topic. Several nanotherapeutics are currently in clinical use that combines features of reduced toxicity and improved circulation.<sup>37</sup> Therapeutic nanoparticles (NPs) in cancer therapy have been approved for several platforms, including liposomes, polymeric micelles, and albumin nanoparticles.<sup>38</sup>

The synthesis method and applications of TSL-IR820-CAT are presented in **Scheme 1**. In this study, the gas-liquid injection technique was designed for precise targeting with a breakthrough skin barrier; TSL-IR820-CAT supplied sufficient oxygen and exerted an enhanced PDT/PTT combined efficacy. As evident from the transmission electron microscopy (TEM) image (**Figure 1A**), the structure of TSL-IR820-CAT was observed, showing a shell-core structure. The same specimen was observed again after being placed for 30 days. The dispersion of TSL-IR820-CAT was still optimal, the size was uniform, and the structure did not change significantly, indicating that the nanoparticles maintained a stable structure for a relatively long time (**Figure 1B**). Dynamic light scattering (DSL) revealed that the average hydrated particle size of TSL-IR820-CAT was 125.3 nm (**Figure 1C**), enabling them to achieve passive targeting by enhancing the EPR.<sup>33</sup> The average zeta potential is displayed in **Figure 1D**, the TSL potential was positively charged, and TSL-IR820 and TSL-IR820-CAT were negatively charged. The average zeta potential of TSL-IR820-CAT was  $-11.0$  mV.



**Scheme 1** Schematic diagram of the synthesis process of TSL-IR820-CAT and the mechanism of enhancing synergistic PDT/PTT antitumor therapy.

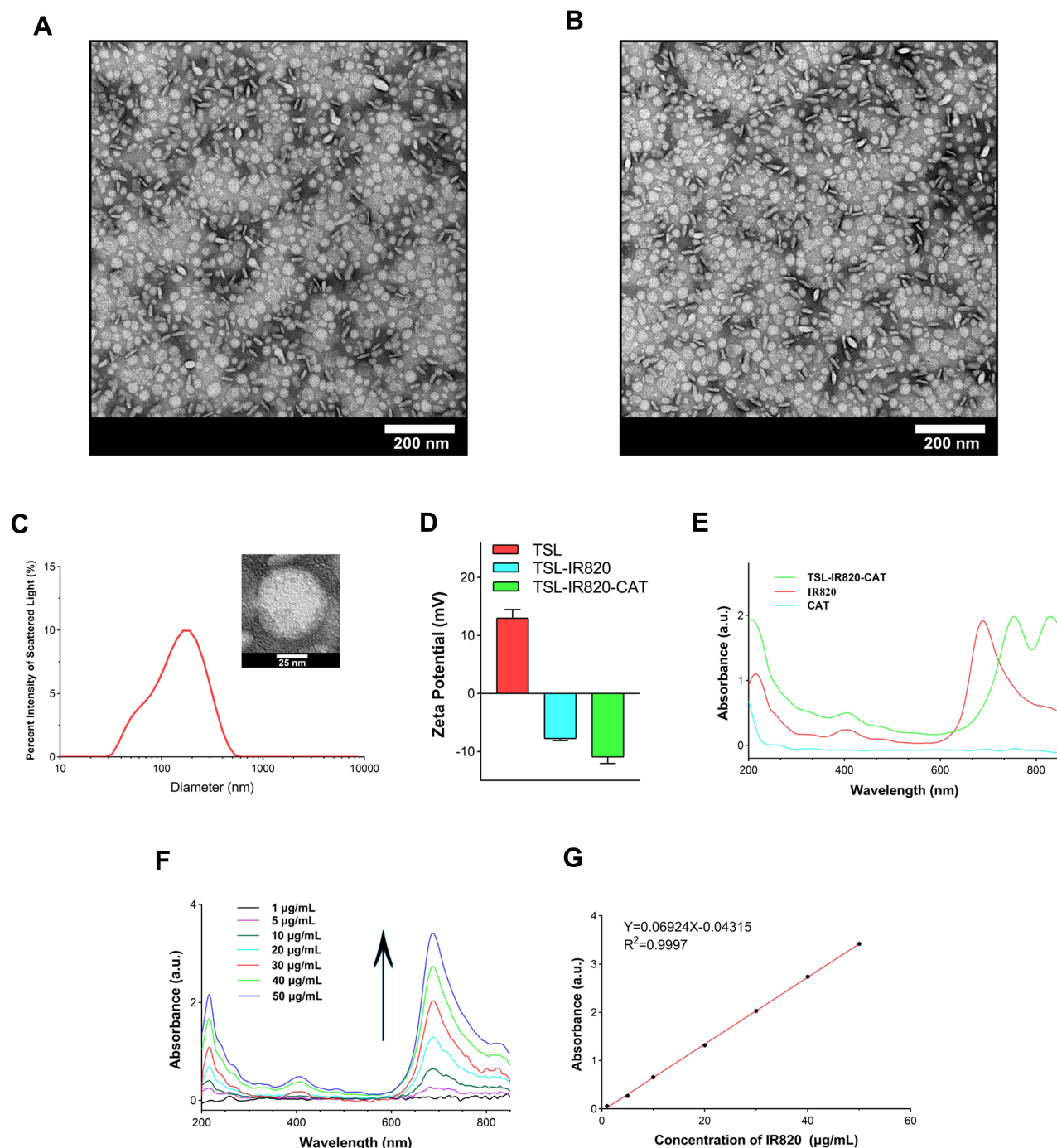


**Figure 1** Characterization of TSL-IR820-CAT. (**A–B**) TEM images of TSL-IR820-CAT ((**A**) and (**B**) represent the same specimen collected at different times). Scale bar: 200 nm. (**C**) Size distribution of TSL-IR820-CAT as measured by dynamic light scattering; inset is a TEM image of an enlarged version of TSL-IR820-CAT. Scale bar: 25 nm. (**D**) Zeta potential results of TSL, TSL-IR820, and TSL-IR820-CAT. (**E**) UV absorption spectra of CAT, IR820, and TSL-IR820-CAT. (**F**) UV absorption spectra of IR820 at different concentrations. (**G**) Spectra of IR820 at the relative absorbance intensity wavelength of 780 nm in the UV absorption spectrum.

The maximum absorption peak of the free IR820 aqueous solution was 690 nm, and that of the CAT aqueous solution was approximately 192 nm. The UV-vis absorption peaks of TSL-IR820-CAT were similar to those of free IR820 and CAT, indicating that the drug was successfully entrapped in nanoliposomes (Figure 1E). To determine the actual content of IR820 and CAT in TSL-IR820-CAT nanoparticles, the standard curves of IR820 (Figures 1F and G) and CAT

(Supplementary Figure S1) were tested, and the encapsulation efficiencies of IR820 and CAT were calculated to be approximately 40.7% and 25.8%, respectively.

## Drug Release and in vitro Photothermal Properties of TSL-IR820-CAT

The fluorescence of calcein was automatically quenched at higher concentrations in the liposomes, but the fluorescence quenching was relieved upon release from the liposomes. The release of c-TINP was detected after 808 nm irradiation. Figure 2A depicts the absorption spectra of calcein at different concentrations, and a standard curve was obtained (Figure 2B). During the photothermal-induced destruction of c-TINPs, calcein was released (Supplementary Figures S2A and S2B). The drug release curve demonstrated that the drug release increased rapidly after 1 min of NIR irradiation. At 10 min, the cumulative release rate of calcein in the c-TINP group reached 78.8%, whereas that in the c-TNP group was 23.6% (Figure 2C). Near-infrared irradiation of IR820-containing nanoparticles can generate high-temperature conditions that facilitate the effective release of their contents.

IR820 can be released from TSL-IR820-CAT after irradiation with near-infrared light, indicating that it can achieve tumor-targeted drug release and exert photodynamic and photothermal therapeutic effects. To assess the photothermal conversion ability of TSL-IR820-CAT, the temperature change under 808 nm near-infrared light was measured. As illustrated in Figures 2D and Supplementary S3A, after 1.5 W/cm<sup>2</sup> near-infrared light irradiation for 6 min, the temperature of TSL-IR820-CAT solution increased as the concentration increased, reaching a maximum temperature of nearly 60 °C, while PBS solution temperatures remained stable. Furthermore, for the TSL-IR820-CAT solution with a fixed concentration of 125 µg/mL, photothermal effects were evaluated under different intensities of near-infrared light irradiation. The TSL-IR820-CAT solution exhibited laser power-dependent photothermal properties, with an elevated temperature of 32.2 °C under irradiation at a power of 1.75 W/cm<sup>2</sup> (Figures 2E and Supplementary S3B). As displayed in Figure 2F, the TEM image of TSL-IR820-CAT heated to 42 °C under NIR irradiation demonstrates that nanostructures

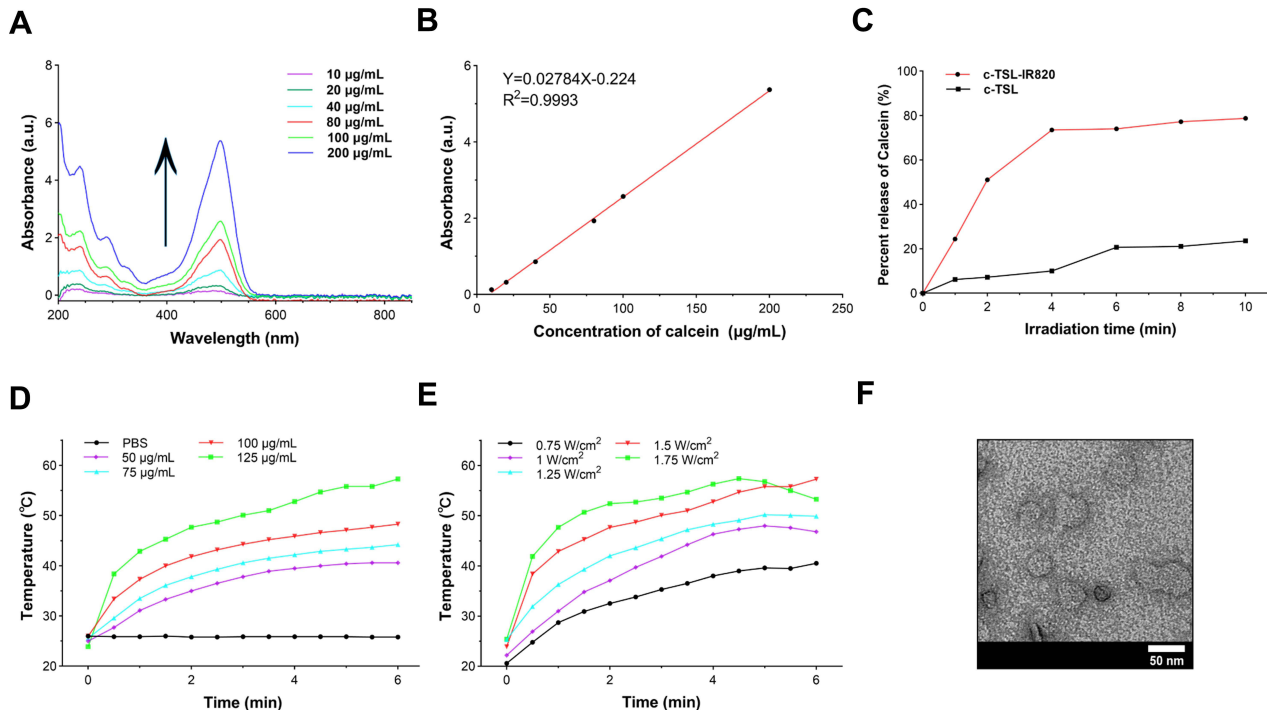


**Figure 2** Drug release and temperature rise characteristics of TSL-IR820-CAT. (A) UV absorption spectra of calcein at different concentrations. (B) Spectra of calcein at the relative absorbance intensity wavelength of 497 nm in the UV absorption spectrum. (C) The rate of calcein release from c-TINP and c-TNP into PBS after irradiation with 808 nm laser (1.5W/cm<sup>2</sup>) for different times. (D) Temperature changes of PBS and suspensions containing different IR820 concentrations of TSL-IR820-CAT under light irradiation (808 nm, 1.5 W/cm<sup>2</sup>). (E) Temperature variation of suspensions of TSL-IR820-CAT under 808 nm lasers at different power densities with a fixed IR820 concentration (125 µg/mL). (F) TEM image of TSL-IR820-CAT heated to 42 °C under NIR irradiation. Scale bar: 50 nm.

were destroyed. The experimental results indicate that TSL-IR820-CAT has optimal photothermal ability and promising potential for photothermal therapy.

## In vitro Cytotoxicity, Cellular Uptake, and Internal Localization of Nanoparticles

Biosafety is essential for developing and researching nanomaterials and their subsequent application in clinical treatment. The cytotoxicity of TSL-IR820-CAT was detected using a CCK8 cytotoxicity detection kit, and the cells used were human skin squamous carcinoma cells A431. As revealed in [Figure 3A](#), when the TSL-IR820-CAT concentration was lower than 125  $\mu\text{g/mL}$ , TSL-IR820-CAT demonstrated no obvious cytotoxicity to A431 cells. When the concentration of TSL-IR820-CAT was increased to 150  $\mu\text{g/mL}$ , the viability of A431 cells was 94.9%, and the cell viability decreased slightly but was still higher than 90.0%. The synthesized TSL-IR820-CAT depicted no obvious toxicity to A431 cells, and its biological safety met the experimental requirements at this stage.

The nanoparticles were labeled with the green fluorescent dye coumarin-6 (f-TICNP), and changes in cell staining with concentration were observed by microscope and flow cytometer. After co-incubation of f-TICNP with A431 cells for 4 h, DAPI solution was applied for 3 min to depict fluorescence of the nuclei. [Figure 3B](#) displays that the nanomaterial (green) enveloped the nucleus (blue), demonstrating that f-TICNP was effectively taken up by A431 cells. Its intake increased with a concentration in a concentration-dependent manner. The flow cytometry results quantified the uptake of A431 cells, and the results were indistinguishable from those obtained by inverted microscopy ([Supplementary Figure S4](#)). The localization of f-TICNP in A431 cells was observed using a confocal laser scanning microscope. As the results demonstrated ([Figures 3C and D](#)), obvious green fluorescence can be seen in A431 cells, the same as the above-mentioned inverted fluorescence microscope and flow cytometry detection results. After co-incubating A431 cells with f-TICNP solution for 4 h, mitochondria were labeled with MitoTracker staining solution (red), and lysosomes were labeled with Lyso-Tracker staining solution (red). Green f-TICNP overlapped with red mitochondria/lysosomes, showing yellow fluorescence, and lysosome staining were more evident than mitochondrial staining ([Figures 3C and D](#)). These results indicate that f-TICNP could be endocytosed into the cell interior through the cell membrane and then transported to the mitochondria and lysosomes of the cell. As mitochondria are sensitive to ROS, this may contribute to the phototoxic effect of PDT.<sup>36</sup>

## Detection of Oxygen Production Characteristics

In PDT, the efficacy is limited by the local hypoxic environment within the tumor, while in CAT, the high concentration of  $\text{H}_2\text{O}_2$  in the tumor tissue can be used to generate oxygen.<sup>39</sup> A red fluorescent dissolved oxygen indicator dye calibrated the oxygen production capacity. The red fluorescence intensity of  $[\text{Ru}(\text{dpp})_3] \text{Cl}_2$  decreased under a microscope and was mainly quenched by oxygen molecules. The intracellular oxygen production capacity of A431 cells treated with nanoparticles was determined using laser confocal microscopy. As displayed in [Figure 4A](#), cells in both the control and TSL-IR820 groups revealed obvious red fluorescence, while the fluorescence intensity of the TSL-IR820-CAT group was significantly reduced. The fluorescence intensity of the TSL-IR820-CAT group was significantly lower than that of the TSL-IR820 group ( $P < 0.01$ ). These results indicated that TSL-IR820-CAT could catalyze oxygen production from  $\text{H}_2\text{O}_2$  present in cells.

HIF-1 is a ubiquitous nuclear protein that is easily controlled by oxygen levels. Its subunit HIF-1 $\alpha$  has been linked to the proliferation and metastasis of tumor cells.<sup>40</sup> In vivo validation must demonstrate hypoxia after the corresponding drug injection by detecting HIF-1 $\alpha$  levels in tissue sites. As illustrated by the staining results in [Figure 4B](#), the expression levels of HIF-1 $\alpha$  in the control and TSL-IR820 groups were higher. The expression of HIF-1 $\alpha$  in the TSL-IR820-CAT group was lower than in the other two groups. These results revealed that TSL-IR820-CAT could generate oxygen in the tumor tissue and improve the hypoxic state of the tumor microenvironment.

## Intracellular ROS Production

Using DCFH-DA as a labeled probe for ROS, ROS production in A431 cells by TSL-IR820-CAT was detected using an inverted fluorescence microscope and flow cytometry. TSL-IR820-CAT can catalyze  $\text{H}_2\text{O}_2$  to generate oxygen, which is used as a ROS source. As illustrated in [Figure 5A](#), the fluorescence intensity of ROS produced by TSL-IR820-CAT was negligible

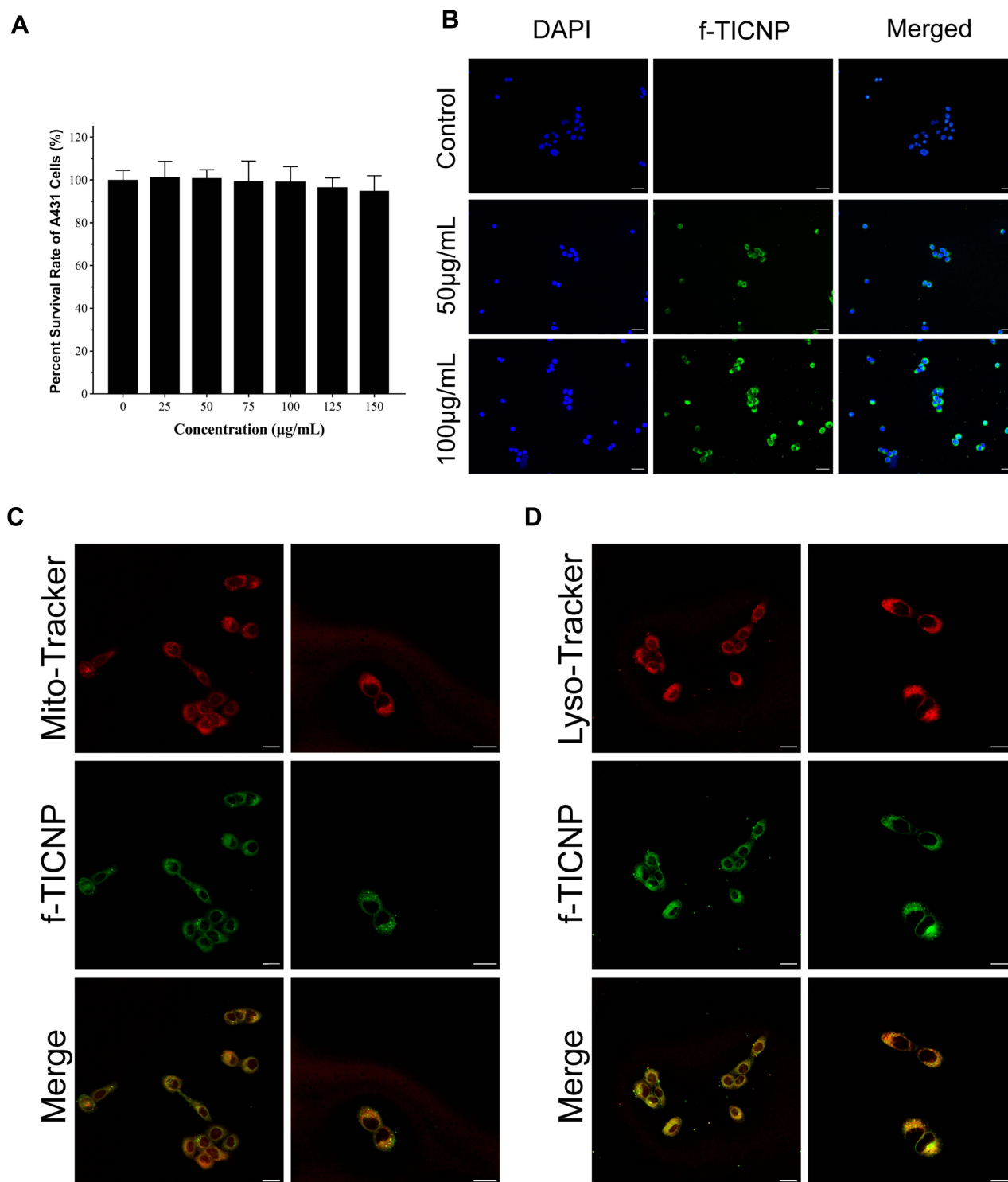


**Figure 3** Safety and colocalization of TSL-IR820-CAT in A431 cells. **(A)** CCK8 assay to determine the cytotoxicity of different concentrations of TSL-IR820-CAT in A431 cells. **(B)** Intracellular uptake of f-TICNP was observed by inverted fluorescence microscopy after incubation with different f-TICNP concentrations. Scale bar: 50 µm. **(C)** Mitochondrial colocalization was observed with CLSM after 4 h incubation with f-TICNP. Scale bar: 20 µm. **(D)** Lysosomal colocalization was visualized with CLSM after 4 h incubation with f-TICNP. Scale bar: 20 µm.

in the absence of laser irradiation and was not significantly different from that of the control group. The intracellular green fluorescence intensities of the PDT and PDT-H<sub>2</sub>O<sub>2</sub> groups were significantly higher than that of the laser-only group. Based on flow cytometry analysis, the fluorescence intensity of ROS in the PDT and PDT-H<sub>2</sub>O<sub>2</sub> groups was significantly higher

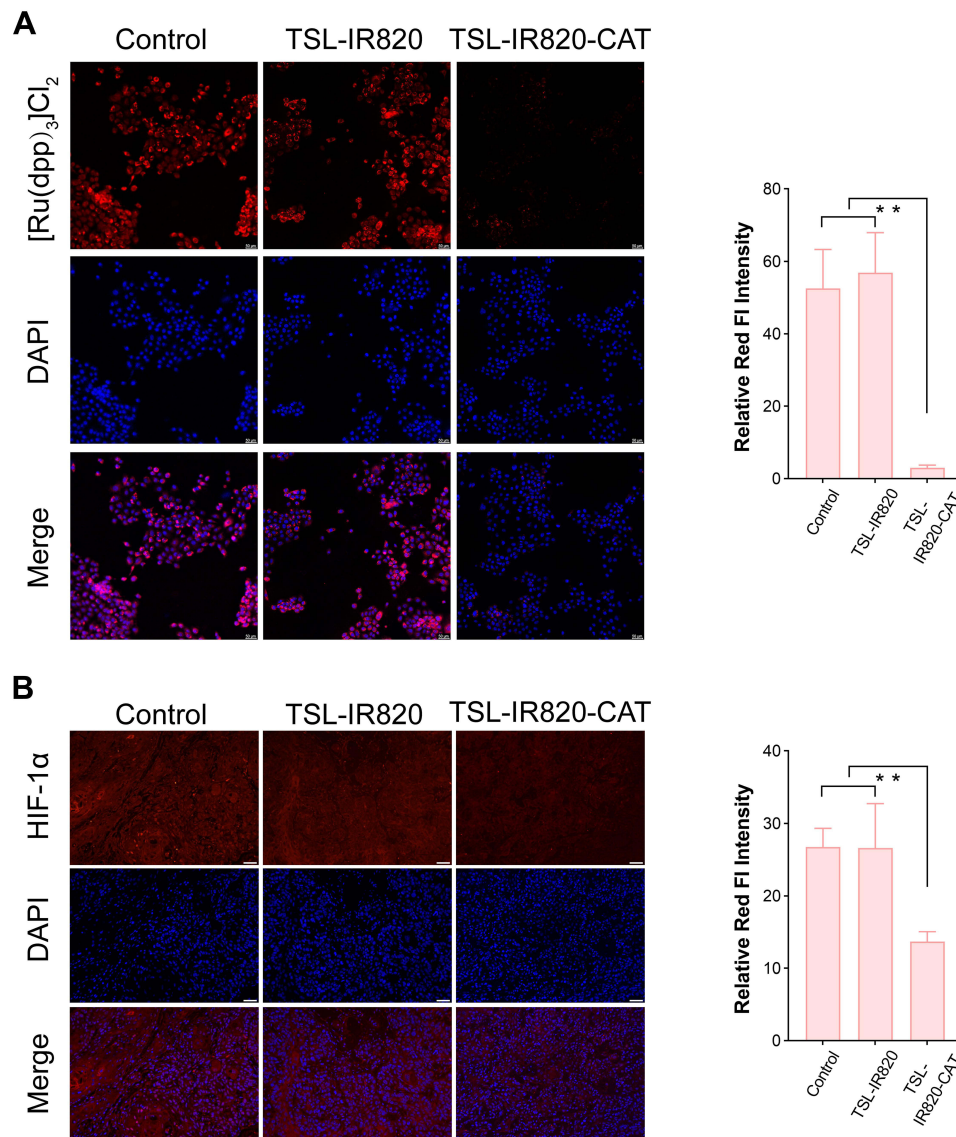


**Figure 4** TSL-IR820-CAT improves hypoxia. **(A)** Oxygen production by TSL-IR820-CAT in A431 cells. Scale bar: 50  $\mu$ m. **(B)** Immunofluorescence staining observation of PBS, TSL-IR820, or TSL-IR820-CAT after needle-free syringe injection to regulate the expression of HIF-1 $\alpha$  in tumor tissue in vivo. Scale bar: 50  $\mu$ m. \*  $P < 0.05$ , \*\*  $P < 0.01$ , \*\*\*  $P < 0.001$ .

than that in the other groups ([Supplementary Figure S5](#)), which is consistent with the above results, indicating that TSL-IR820-CAT mediated PDT effects can effectively generate ROS to exert the antitumor effect of PDT.

## In vitro Synergistic Antitumor Efficacy of TSL-IR820-CAT

To evaluate the in vitro therapeutic effect of TSL-IR820-CAT, live and dead cell staining experiments were used for validation. Cells were stained with calcein-AM/PI; live cells demonstrated green fluorescence, whereas dead cells displayed red fluorescence. In the PDT group, laser irradiation was performed under ice incubation. A431 cells were pretreated with vitamin C in the PTT group to remove ROS.<sup>41,42</sup> As presented in the results in [Figure 5B](#), the cells in control and laser-only groups had normal morphology and no apparent cell death, consistent with the results of the CCK8 experiment, indicating that the nanoparticles had optimal biocompatibility. In the PDT group, some cells died after laser irradiation, and approximately half of the cells survived. In the PTT group, the number of dead cells further increased. More importantly, the red fluorescent spots in the full field of view could be seen under the microscope of the treated cells in the PDT+PTT group, indicating a significant tumor-killing effect.

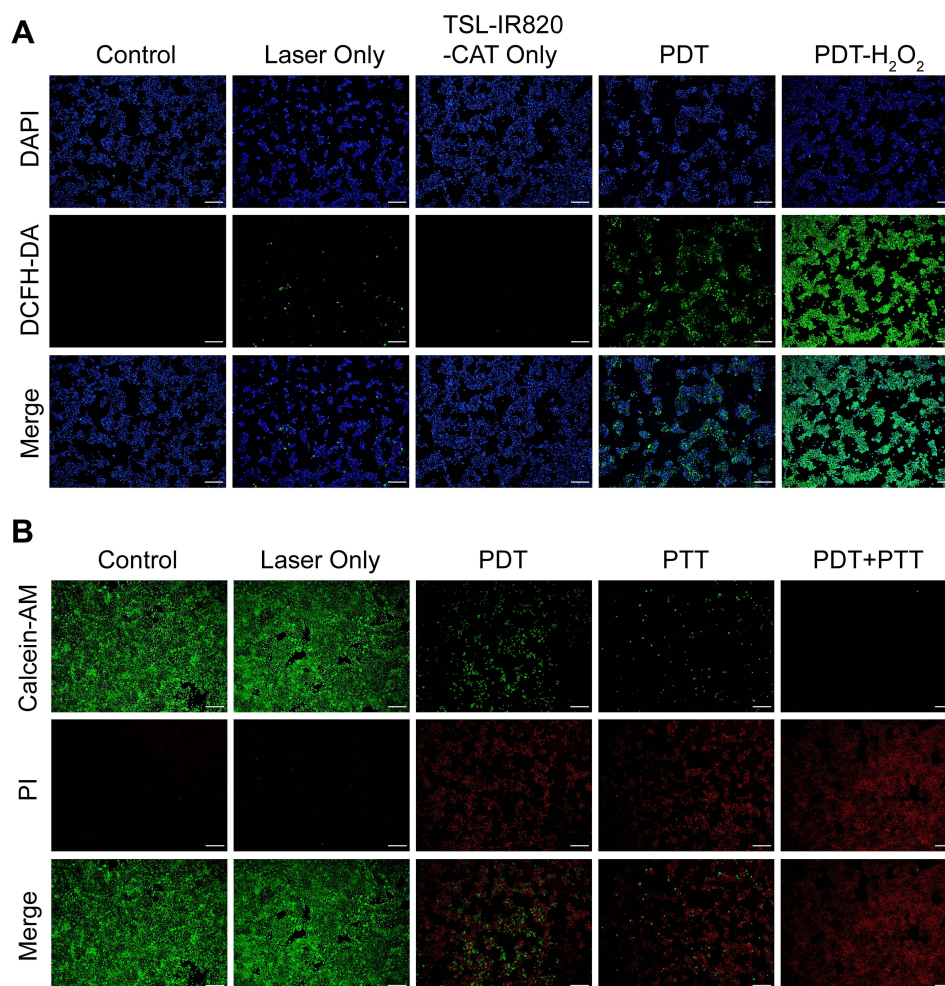


**Figure 5** PDT and PTT effects of TSL-IR820-CAT in A431 cells. **(A)** Fluorescence microscopy images of ROS generated by different treatments (blue fluorescence represents nuclear localization, green fluorescence represents ROS-positive staining). Scale bar: 200  $\mu$ m. **(B)** Fluorescence microscopy images of A431 cells stained with Calcein AM/PI for five groups of treatments (green fluorescence represents live cells, red fluorescence represents dead cells). Scale bar: 200  $\mu$ m.

## In vivo FI Imaging

TSL-IR820-CAT is required to accumulate within tumors to enhance tumor suppression. Therefore, fluorescence imaging confirmed the in vivo distribution of the nanoparticles injected through a needle-free syringe. The fluorescent dye coumarin-6 labeled nanoparticle f-TICNP was used to observe the fluorescence images of A431 skin squamous cell carcinoma tumor-bearing nude mice. At irradiation times of 0.5, 2, 4, and 6 h, it was evident that with time, the fluorescence in the tumor area became more concentrated, and the signal did not weaken (Figure 6A). Moreover, the tumor, heart, liver, spleen, lung, and kidney were collected from the mice after 6 h of observation to further observe the metabolism and aggregation of nanomaterials. As illustrated in Figures 6B and C, the fluorescence signal intensity of the tumor tissue was the most obvious, and a small amount of fluorescence signal existed in the liver and kidney, indicating the metabolic pathway of the nanoparticles.

## In vivo Photothermal and the Efficacy of Dual Therapy

The barrier between the inside and outside of the skin is mainly composed of the stratum corneum, but hyperkeratosis is often seen in skin tumors and precancerous lesions.<sup>43,44</sup> The direct application of photosensitizers to the skin is difficult, which impedes their absorption of photosensitizers. To overcome the insufficient penetration depth and uneven diffusion

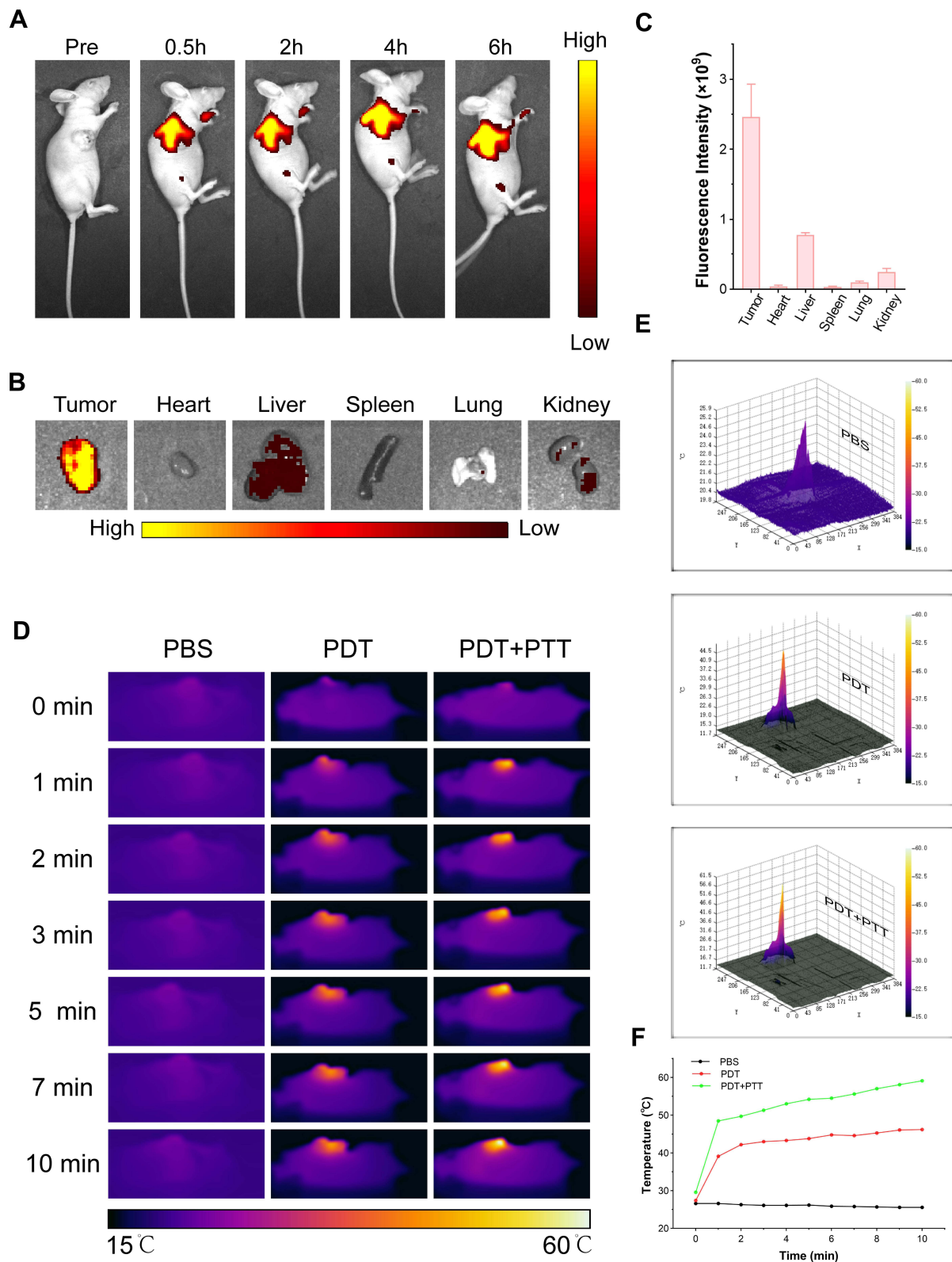


**Figure 6** (A) Fluorescence imaging of A431 squamous cell carcinoma tumor-bearing nude mice after needle-free syringe injection of f-TICNP. (B) Graph of ex vivo fluorescence signals detected in tumors and major organs 6 h after needle-free syringe injection. (C) Infrared thermographic images of A431 squamous cell carcinoma nude mice at different time points were collected by NIR laser irradiation (1 or 1.5 W/cm<sup>2</sup>) for 10 min after injecting PBS and TSL-IR820-CAT with a needle-free syringe, respectively. (D) 3D IR photothermal images of tumor sites in mice treated with PBS, PDT, and PDT+PTT at 10 min, respectively. (E) The corresponding real-time temperature changes during NIR laser irradiation of the tumor site. \* P < 0.05, \*\* P < 0.01, \*\*\* P < 0.001.

of photosensitizers in treating skin tumors, a German INJEX needle-free syringe was employed in this study. TSL-IR820-CAT was injected into the tumor tissue area of tumor-bearing mice using a needleless syringe, and temperature changes were recorded using a thermal imager. After 10 min of 1.5 W/cm<sup>2</sup> laser irradiation, the body temperature of the tumor site in the PDT + PTT group increased rapidly to 59.1°C, which exceeded the irreversible temperature in inducing tumor ablation (Figure 6D). The rapid increase in temperature over a short period was attributed to the targeted aggregation of nanoparticles after needle-free injection.

In contrast, the temperature of the tumor site in the PDT group reached 46.2 °C after 10 min of laser irradiation at 1W/cm<sup>2</sup>, which was much lower than that in the PDT + PTT group. As displayed in Figure 6E, the corresponding 3D photothermal images of PBS, PDT, and PDT + PTT provided a three-dimensional analysis for determining the temperature of mouse tumors. Temperature changes from the central region of the tumor to its borders can be observed more intuitively. No noticeable increase in the tumor temperature was observed in the PBS group (Figure 6F). These results indicated that TSL-IR820-CAT could provide significant PDT and PTT effects *in vitro*.

Next, we explored the antitumor efficacy of TSL-IR820-CAT in an orthotopic A431 cutaneous squamous cell carcinoma mouse model based on circulation time and enhanced tumor targeting. The treatment regimen followed the schedule illustrated in Figure 7A. The comparison of tumor volume and weight of tumor-bearing mice between separate groups directly reflects the efficacy of antitumor therapy. The trend of the treatment effect in tumor-bearing mice was evident on the 12th day after the different treatments (Figure 7B). The tumor growth status demonstrated that the volume increased rapidly with time in the control and laser-only groups. After treatment in the PDT and PTT groups, the growth rate of the tumor slowed but still revealed a continuous growth trend. Tumor growth in the PDT+PTT group was significantly inhibited (Figure 7E). Tumors from the dissected mice were weighed and recorded after completing the treatment cycle (Figures 7C and D). The results revealed differences in tumors among the groups, with the PDT+PTT group having almost no tumors on day 18, consistent with the tumor growth curve results.

The TUNEL assay and H&E staining were used to further evaluate the ability of TSL-IR820-CAT-mediated PDT/PTT combination therapy to induce apoptosis in mice. TUNEL staining of tumor tissue in Figure 7F displays that the control and laser-only groups were negative. The positive areas of the PDT and PTT groups were higher than those of the control and laser-only groups. However, many residual tumor cells continue to grow and develop, leading to recurrence. The positive area in the PDT + PTT group was significantly more extensive than in the other four groups. H&E staining of tumor tissues led to the same conclusion (Figure 7F). TSL-IR820-CAT was successfully transported into tumor cells and enhanced the antitumor effects of PDT/PTT.

## Long-Term Biosafety of TSL-IR820-CAT

By measuring the H&E staining of the major organs after the treatment cycle and by measuring the weight of mice during the biological safety of the treatment cycle, the TSL-IR820-CAT treatment system was evaluated for biological safety. Compared with the control group, after 18 days of PDT combined with PTT treatment, no pathological differences were observed in the tissue sections of the main organs of the mice in each group under a microscope (Supplementary Figure S6). Supplementary Figure S7 depicts that all mice did not lose significant body weight during the weighing procedure. The results indicate that TSL-IR820-CAT, mediated by a needle-free syringe, has no systemic toxicity and offers qualified biosafety and considerable therapeutic potential.

## Conclusions

The TSL-IR820-CAT nanoreactor was successfully developed to deliver partially mitochondria-targeted and oxygen-rich PDT directly into the tumor interior with a needle-free syringe and achieved simultaneous PDT/PTT for a single near-infrared treatment. TSL acts as a “gatekeeper” by preventing premature release of IR820 and CAT integrated with its core until the TSL phase transition temperature is reached. Using this strategy, hypoxia is effectively alleviated in the tumor microenvironment, and hyperkeratosis of the skin due to squamous cell carcinoma does not interfere with the penetration of photothermal agents or photosensitizers. Under 808 nm laser irradiation, the enhanced combined antitumor effect of

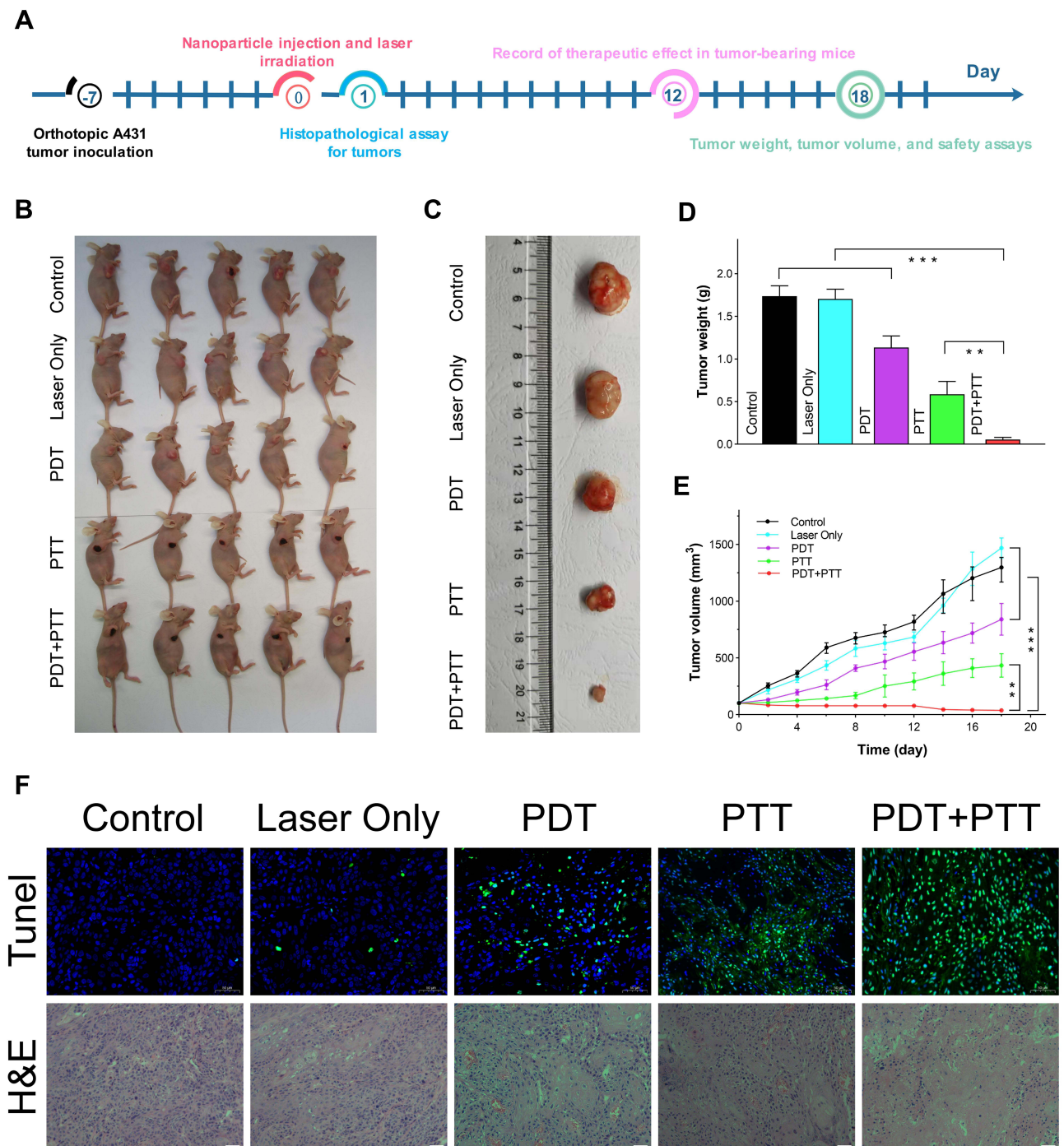


**Figure 7** In vivo anti-squamous cell carcinoma after TSL-IR820-CAT injection by needle-free syringe. **(A)** Schematic diagram of the treatment regimen. **(B)** Tumor photographs of five groups of tumor-bearing mice were taken on the 12th day after different treatments. **(C)** Tumor anatomy photos of mice in five groups after different treatments. **(D)** The observed tumor tissue weight after 18 days of treatment. **(E)** After different treatments, the tumor growth curves of the five groups are observed. **(F)** TUNEL and H&E staining of different treatment groups. Scale bar: 50  $\mu$ m. \*  $P < 0.05$ , \*\*  $P < 0.01$ , \*\*\*  $P < 0.001$ .

PDT/PTT breaks the bottleneck of existing treatment modalities; that is, the treatment effect is insufficient due to a single treatment modality. This study aimed to maximize the antitumor efficacy of PDT and PTT, expand the scope of needle-free syringe applications, and develop an innovative method for treating squamous cell carcinoma.

## Disclosure

The authors report no conflicts of interest in this work.

## References

1. Liu P, Zhou Y, Shi X, et al. A cyclic nanoreactor achieving enhanced photodynamic tumor therapy by reversing multiple resistances. *J Nanobiotechnology*. 2021;19(1):149. doi:10.1186/s12951-021-00893-6
2. Meng X, Zhang B, Yi Y, et al. Accurate and real-time temperature monitoring during MR imaging guided PTT. *Nano Lett*. 2020;20(4):2522–2529. doi:10.1021/acs.nanolett.9b05267
3. Xu Q, Li D, Zhou H, et al. MnO<sub>2</sub>-coated porous Pt@CeO<sub>2</sub> core-shell nanostructures for photoacoustic imaging-guided tri-modal cancer therapy. *Nanoscale*. 2021;13(39):16499–16508. doi:10.1039/d1nr03246a
4. Ghayyem S, Barras A, Faridbod F, Szunerits S, Boukherroub R. Effective PDT/PTT dual-modal phototherapeutic killing of bacteria by using poly (N-phenylglycine) nanoparticles. *Mikrochim Acta*. 2022;189(4):150. doi:10.1007/s00604-022-05181-0
5. Li M, Li S, Zhou H, et al. Chemotaxis-driven delivery of nano-pathogenoids for complete eradication of tumors post-phototherapy. *Nat Commun*. 2020;11(1):1126. doi:10.1038/s41467-020-14963-0
6. Zhai Y, Wang J, Qiu L. Drug-driven self-assembly of pH-sensitive nano-vesicles with high loading capacity and antitumor efficacy. *Biomater Sci*. 2021;9(9):3348–3361. doi:10.1039/d0bm01987a
7. Aizik G, Waiskopf N, Agbaria M, et al. Liposomes of quantum dots configured for passive and active delivery to tumor tissue. *Nano Lett*. 2019;19(9):5844–5852. doi:10.1021/acs.nanolett.9b01027
8. Jiang Y, Meng W, Wu L, et al. Image-guided TME-improving nano-platform for Ca<sup>2+</sup> signal disturbance and enhanced tumor PDT. *Adv Healthc Mater*. 2021;10(19):e2100789. doi:10.1002/adhm.202100789
9. Sun J, Wan Z, Xu J, et al. Tumor size-dependent abscopal effect of polydopamine-coated all-in-one nanoparticles for immunochemo-photothermal therapy of early- and late-stage metastatic cancer. *Biomaterials*. 2021;269:120629. doi:10.1016/j.biomaterials.2020.120629
10. Jones AT, Shen X, Walter KL, et al. HIV-1 vaccination by needle-free oral injection induces strong mucosal immunity and protects against SHIV challenge. *Nat Commun*. 2019;10(1):798. doi:10.1038/s41467-019-08739-4
11. Ocak H, Akkoyun EF, Çolpak HA, et al. Is the jet injection effective for teeth extraction? *J Stomatol Oral Maxillofac Surg*. 2020;121(1):19–24. doi:10.1016/j.jormas.2019.05.001
12. Mu X, Wang L, Wang L, Ge R, Dang H, Mou K. Plum-blossom needling enhanced the effect of photodynamic therapy on basal cell carcinoma. *Photodiagn Photodyn Ther*. 2018;23:339–341. doi:10.1016/j.pdpdt.2018.08.001
13. Zhao W, Tian X, Fang Z, et al. Engineering single-molecule fluorescence with asymmetric nano-antennas. *Light Sci Appl*. 2021;10(1):79. doi:10.1038/s41377-021-00522-9
14. Li J, Liu H, Fu T, Wang R, Zhang X, Tan W. Recent progress in small-molecule near-ir probes for bioimaging. *Trends Chem*. 2019;1(2):224–234. doi:10.1016/j.trechm.2019.03.002
15. Han Z, Tu X, Qiao L, et al. Phototherapy and multimodal imaging of cancers based on perfluorocarbon nanomaterials. *J Mater Chem B*. 2021;9(34):6751–6769. doi:10.1039/d1tb00554e
16. Zhang G, Cheng W, Du L, Xu C, Li J. Synergy of hypoxia relief and heat shock protein inhibition for phototherapy enhancement. *J Nanobiotechnology*. 2021;19(1):9. doi:10.1186/s12951-020-00749-5
17. Mkhobongo B, Chandran R, Abrahamse H. The role of melanoma cell-derived exosomes (MTEX) and photodynamic therapy (PDT) within a tumor microenvironment. *Int J Mol Sci*. 2021;22(18):9726. doi:10.3390/ijms22189726
18. Cramer GM, Cengel KA, Busch TM. Forging forward in photodynamic therapy. *Cancer Res*. 2022;82(4):534–536. doi:10.1158/0008-5472.CAN-21-4122
19. Hou X, Tao Y, Pang Y, Li X, Jiang G, Liu Y. Nanoparticle-based photothermal and photodynamic immunotherapy for tumor treatment. *Int J Cancer*. 2018;143(12):3050–3060. doi:10.1002/ijc.31717
20. Feng L, Li C, Liu L, et al. Acceptor planarization and donor rotation: a facile strategy for realizing synergistic cancer phototherapy via type I PDT and PTT. *ACS Nano*. 2022;16(3):4162–4174. doi:10.1021/acsnano.1c10019
21. Yang H, Xu B, Li S, et al. A photoresponsive nanozyme for synergistic catalytic therapy and dual phototherapy. *Small*. 2021;17(10):e2007090. doi:10.1002/smll.202007090
22. Huang X, Lu Y, Guo M, Du S, Han N. Recent strategies for nano-based PTT combined with immunotherapy: from a biomaterial point of view. *Theranostics*. 2021;11(15):7546–7569. doi:10.7150/thno.56482
23. Han R, Xiao Y, Yang Q, et al. Ag<sub>2</sub>S nanoparticle-mediated multiple ablations reinvigorates the immune response for enhanced cancer photo-immunotherapy. *Biomaterials*. 2021;264:120451. doi:10.1016/j.biomaterials.2020.120451
24. Tang L, Xiao Q, Yin Y, et al. An enzyme-responsive and NIR-triggered lipid-polymer hybrid nanoplatfor for synergistic photothermal/chemo cancer therapy. *Biomater Sci*. 2022;10(9):2370–2383. doi:10.1039/d2bm00216g
25. Liu P, Yang W, Shi L, et al. Concurrent photothermal therapy and photodynamic therapy for cutaneous squamous cell carcinoma by gold nanoclusters under a single NIR laser irradiation. *J Mater Chem B*. 2019;7(44):6924–6933. doi:10.1039/c9tb01573f
26. Wu H, Wang W, Zhang Z, et al. Synthesis of a clay-based nanoagent for photonanomedicine. *ACS Appl Mater Interfaces*. 2020;12(1):390–399. doi:10.1021/acsami.9b19930
27. Regenold M, Steigenberger J, Siniscalchi E, et al. Determining critical parameters that influence in vitro performance characteristics of a thermosensitive liposome formulation of vinorelbine. *J Control Release*. 2020;328:551–561. doi:10.1016/j.jconrel.2020.08.059
28. Du C, Li S, Li Y, et al. F7 and topotecan co-loaded thermosensitive liposome as a nano-drug delivery system for tumor hyperthermia. *Drug Deliv*. 2020;27(1):836–847. doi:10.1080/10717544.2020.1772409
29. Di J, Xie F, Xu Y. When liposomes met antibodies: drug delivery and beyond. *Adv Drug Deliv Rev*. 2020;154:151–162. doi:10.1016/j.addr.2020.09.003
30. Rhoo GC, Franckena M, Hagen TLMT. A moderate thermal dose is sufficient for effective free and TSL based thermochemotherapy. *Adv Drug Deliv Rev*. 2020;163:145–156. doi:10.1016/j.addr.2020.03.006

31. Tang J, Zhou H, Hou X, et al. Enhanced antitumor efficacy of temozolomide-loaded carboxylated poly (amido-amine) combined with photothermal/photodynamic therapy for melanoma treatment. *Cancer Lett.* 2018;423:16–26. doi:10.1016/j.canlet.2018.03.002
32. Hou X, Zhou H, Wang L, et al. Multifunctional near-infrared dye-magnetic nanoparticles for bioimaging and cancer therapy. *Cancer Lett.* 2017;390:168–175. doi:10.1016/j.canlet.2016.12.026
33. Wu B, Wan B, Lu S, et al. Near-infrared light-triggered theranostics for tumor-specific enhanced multimodal imaging and photothermal therapy. *Int J Nanomedicine.* 2017;12:4467–4478. doi:10.2147/IJN.S137835
34. Wang S, Xin J, Zhang L, et al. Cantharidin-encapsulated thermal-sensitive liposomes coated with gold nanoparticles for enhanced photothermal therapy on A431 cells. *Int J Nanomedicine.* 2018;13:2143–2160. doi:10.2147/IJN.S156240
35. Zahiri M, Taghavi S, Abnous K, Taghdisi SM, Ramezani M, Alibolandi M. Theranostic nanobubbles towards smart nanomedicines. *J Control Release.* 2021;339:164–194. doi:10.1016/j.jconrel.2021.09.032
36. Tian J, Huang B, Cu Z, et al. Mitochondria-targeting and ROS-sensitive smart nanoscale supramolecular organic framework for combinational amplified photodynamic therapy and chemotherapy. *Acta Biomater.* 2021;130:447–459. doi:10.1016/j.actbio.2021.05.048
37. Shi J, Kantoff PW, Wooster R, Farokhzad OC. Cancer nanomedicine: progress, challenges and opportunities. *Nat Rev Cancer.* 2017;17(1):20–37. doi:10.1038/nrc.2016.108
38. Kim B, Park JE, Im E, et al. Recent advances in nanotechnology with nano-phytochemicals: molecular mechanisms and clinical implications in cancer progression. *Int J Mol Sci.* 2021;22(7):3571. doi:10.3390/ijms22073571
39. Zhou X, You M, Wang F, et al. Multifunctional graphdiyne-cerium oxide nanozymes facilitate MicroRNA delivery and attenuate tumor hypoxia for highly efficient radiotherapy of esophageal cancer. *Adv Mater.* 2021;33(24):e2100556. doi:10.1002/adma.202100556
40. Li T, Mao C, Wang X, Shi Y, Tao Y. Epigenetic crosstalk between hypoxia and tumor driven by HIF regulation. *J Exp Clin Cancer Res.* 2020;39(1):224. doi:10.1186/s13046-020-01733-5
41. Zhang L, Wang D, Yang K, et al. Mitochondria-targeted artificial “Nano-RBCs” for amplified synergistic cancer phototherapy by a single NIR irradiation. *Adv Sci.* 2018;5(8):1800049. doi:10.1002/advs.201800049
42. Sun CX, Ma YJ, Wang JW. Improved hypocrellin A production in *Shiraia bambusicola* by light-dark shift. *J Photochem Photobiol B.* 2018;182:100–107. doi:10.1016/j.jphotobiol.2018.04.004
43. Krishnan V, Mitragotri S. Nanoparticles for topical drug delivery: potential for skin cancer treatment. *Adv Drug Deliv Rev.* 2020;153:87–108. doi:10.1016/j.addr.2020.05.011
44. Erlendsson AM, Olesen UH, Haedersdal M, Rossi AM. Ablative fractional laser-assisted treatments for keratinocyte carcinomas and its precursors-Clinical review and future perspectives. *Adv Drug Deliv Rev.* 2020;153:185–194. doi:10.1016/j.addr.2020.01.001

International Journal of Nanomedicine

Dovepress

## Publish your work in this journal

The International Journal of Nanomedicine is an international, peer-reviewed journal focusing on the application of nanotechnology in diagnostics, therapeutics, and drug delivery systems throughout the biomedical field. This journal is indexed on PubMed Central, MedLine, CAS, SciSearch<sup>®</sup>, Current Contents<sup>®</sup>/Clinical Medicine, Journal Citation Reports/Science Edition, EMBase, Scopus and the Elsevier Bibliographic databases. The manuscript management system is completely online and includes a very quick and fair peer-review system, which is all easy to use. Visit <http://www.dovepress.com/testimonials.php> to read real quotes from published authors.

Submit your manuscript here: <https://www.dovepress.com/international-journal-of-nanomedicine-journal>